Korean J. Chem. Eng., 37(12), 2143-2151 (2020)
DOI: 10.1007/s11814-020-0647-6

pISSN: 0256-1115
eISSN: 1975-7220

Synthesis of high-performance Ni/$Ce_{0.8}Zr_{0.2}O_2$ catalyst via co-nanocasting method for ethanol dry reforming

Guangyu Shi, Yuanhao Wang, Yafeng Cao, Weijie Cai†, and Fengzhi Tan†

School of Light Industry and Chemical Engineering, Dalian Polytechnic University, Dalian 116034, China

(*Received 16 April 2020 • Revised 20 July 2020 • Accepted 27 July 2020*)

Abstract−A Ni/$Ce_{0.8}Zr_{0.2}O_2$ catalyst (NiCeZr-N) was synthesized by a facile co-nanocasting technique for syngas production from ethanol dry reforming. In addition, a series of characterization techniques, such as transmission electron microscopy (TEM), X-ray diffraction (XRD), inductive coupled plasma Emission Spectrometer (ICP), X-ray photoelectron spectroscopy (XPS), Raman and hydrogen temperature programmed reduction (H_2-TPR) were selected to evaluate the physicochemical features of the as-prepared catalysts. Indeed, the results indicated that NiCeZr-N catalyst prepared by co-nanocasting method had a smaller particle size (<5 nm), relatively higher specific surface area (39 m^2/g) and stronger metal-support interaction in comparison with another model catalyst obtained from conventional co-precipitation method (NiCeZr-P). Expectedly, these positive factors enabled NiCeZr-N catalyst to exhibit better activity and stability. Typically, ethanol is completely converted by using NiCeZr-N as catalyst and heating to 700 °C, and CO_2 conversion was as high as 65.3%. Interestingly, H_2/CO was close to 1.1 at 650 °C, which could be used as feedstocks of Fischer-Tropsch process. Particularly, no obvious fluctuation of ethanol conversion and the product selectivity was observed during 40 h time-on-stream stability test.

Keywords: Ni/$Ce_{0.8}Zr_{0.2}O_2$, Co-nanocasting, Ethanol Dry Reforming, Syngas

INTRODUCTION

In recent decades, the large-scale utilization of fossil fuels has led to the enormous CO_2 emission, an undesirable greenhouse gas [1-3]. Hence, great endeavours, such as conventional physical sequestration and the attractive chemical utilization have been conducted to deal with the CO_2 pollution. Particularly, ethanol dry reforming (DRE), a process converting the undesirable CO_2 into the value-added syngas, has been regarded as one of the most promising solutions. Actually, enormous high-valued chemicals can be produced from syngas via Fischer-Tropsch process [1,2]. Bio-ehanol can be derived either from starch or biomass residue such as corn straw, bagasse, rice straw, and maguey [4]. Moreover, ethanol is biodegradable, non-toxic, sulfur-free, and renewable [1,4]. In 2018, the total production of ethanol reached 28,700 million gallons [4]. Hence, as a product of renewable materials, the selection of ethanol as the reactant for dry reforming process could greatly meet sustainable development instead of the conventional methane dry reforming.

To date, the developed common catalysts for dry reforming reaction have been mainly classified as transition metals (Ni, Co, Cu) and/or noble metals (Ir, Ru, Rh, Pd) [5-7]. It has been generally accepted that noble metal based catalysts exhibit good activity and stability for catalytic dry reforming reactions. Zhao et al. reported that complete ethanol and 70% of CO_2 conversion were achieved over Rh/CeO_2 catalyst and syngas was the major product with H_2/CO ration of 0.9 [8]. Dirf et al. demonstrated the effect of support on DRE performance by utilizing binary oxides of Al_2O_3 with ZrO_2, NiO, MgO, CeO_2 or La_2O_3 [9]. The experimental results indicated that the catalytic behavior of the Rh-based catalysts decreased in the order of Rh/NiO-Al_2O_3>>Rh/Al_2O_3≈Rh/MgO-Al_2O_3≈Rh/CeO_2-Al_2O_3≈Rh/ZrO_2-Al_2O_3≈Rh/La_2O_3-Al_2O_3 [9]. However, the high cost of noble metal greatly limited its industrial research and application [10,11]. On the other hand, Ni, as one of the low-cost transition metals, possesses a stronger dissociation capacity for C-C bond and O-H bond in comparison with Fe and Co; therefore, Ni-based catalysts present attractive catalytic activity for DRE reaction [12]. Samsudeen et al. investigated the effect of calcination temperature on the catalytic performance of 10 wt% Ni/Al_2O_3 catalysts. The results showed that CO_2 conversion reached 57% at 600 °C, and H_2 selectivity remained constant at *ca.* 50% [13]. However, nickel was prone to deactivation due to the serious carbon deposition and its easy sintering features, which prevented its large-scale industrial application [14,15]. Hence, various methods have been designed to improve the resistance to coke formation and sintering of nickel-based catalysts [16]. Bej et al. indicated that alumina supported nano-NiO-SiO_2 catalyst was more stable than the commercial catalyst in the study [17]. To investigate possible improvements in their DRE activity and stability, Ni-based catalysts were promoted by the addition of several components such as Ce, Co and La [1,18]. Wei et al. synthesized a Ni/KIT-6 catalyst with the highly uniform Ni dispersion by a facile methanol-assisted co-impregnation technique. The experimental results showed that the presence of the samller Ni particles and the stronger Ni-support interaction in the Ni/KIT-6 catalyst corresponded to its better activity and stability compared to the Ni/SiO_2 samples [19].

---

†To whom correspondence should be addressed.
E-mail: caiwj@dlpu.edu.cn, tanfz@dlpu.edu.cn

It was accepted that co-nanocasting was a highly efficient technique to synthesize the nano-materials with the typical nanostructure [20]. Co-nanocasting process provided a limited nanoreactor for the formation of Ni oxide which kept the Ni oxides with small particle size, high surface area, rich surface adsorbed oxygen species, low temperature reducibility and promoting metal-suppoort interaction in Ni-Ce-Zr [21]. Considering that the dispersion and particle size of the active components on the support surface are closely related to the catalytic performance, co-nanocasting technology has attracted more attention to prepare the catalysts with high specific surface area and small metal particle size [22,23]. Duan et al. synthesized a type of ordered mesoporous $LaNiO_3$ perovskite oxide via a modified co-nanocasting method for partial oxidation of methane (POM) reaction [24]. The synthesized catalyst had a smaller nickel particle size and larger specific surface area, which effectively prevented metal sintering and carbon deposition of the catalyst. Valdés-Solís et al. prepared an active CuO/ZnO catalyst by co-nanocasting technology using a mesoporous active carbon as template for the steam reforming of methanol (SRM) [25]. Sousa et al. described the performance of nanostructured spinel Ni- and Co-based catalysts and showed that the resistance to coking in DRM reaction was more likely due to the participation function of nanocrystalline $NiAl_2O_4$ [26]. Xu et al. synthesized a Cu-based catalyst by active carbon co-nanocasting technology for SRM. The catalyst exhibited a satisfactory activity which showed ~86.1% methanol conversion as well as 74.6 mol% H_2 concentration. Nonetheless, methanol conversion decreased to *ca.* 73.3% together with 69.4 mol% H_2 for another catalyst synthesized by conventional coprecipitation method [27].

With respect to catalyst support, the inhibition effect of CeO_2-ZrO_2 composite oxides on the carbon deposition could be anticipated. Oxygen storage capacity is widely known as a characteristic of CeO_2 [28,29]. The oxygen storage capacity of CeO_2 resulted from the rapid and reversible redox reaction between Ce^{4+} and Ce^{3+}. However, CeO_2 generally showed poor thermal stability, which might lead to rapid catalyst deactivation because of the decline of oxygen storage capacity. Zr dopant can effectively improve the oxygen mobility and thermal stability of CeO_2, thus preventing the sintering of the catalysts [30]. On the other hand, the strong interaction between CeO_2-ZrO_2 composite oxides and Ni can stabilize the active metal particles on the support and thereby delay its sintering [31].

In this paper, two Ni-based catalysts were prepared by conventional coprecipitation method (NiCeZr-P) and co-nanocasting techniques (NiCeZr-N), respectively. The effect of co-nanocasting technology on the particle size of Ni and the physicochemical properties were deeply investigated, and its catalytic performance for DRE reaction was also evaluated. The catalysts were characterized by automatic surface area and porosity analyzer, TEM, XRD, XPS, Raman, H_2-TPR and ICP to establish the relationship between catalyst structure and catalytic performance.

MATERIALS AND METHODS

1. Materials

Coconut shell based activated carbon was purchased from Jiangsu Xinghong Carbon Industry Technology Co. Ltd. (Yixing, China), and dried at 100 °C for 24 h. Sodium carbonate and ethanol were purchased from the Kermel Chemical Reagent Co. Ltd. (Tianjin China). Nickel(II) nitrate hexahydrate ($Ni(NO_3)_2{\cdot}6H_2O$), Cerium(III) nitrate hexahydrate ($Ce(NO_3)_3{\cdot}6H_2O$) and Zirconyl chloride octahydrate ($ZrOCl_2{\cdot}8H_2O$) were purchased from Aladdin Industrial Corporation (Shanghai China). All chemical reagents were of analytical grade and directly used without further purification.

2. Catalyst Preparation

5 wt% Ni/$Ce_{0.8}Zr_{0.2}O_2$ (Ce/Zr=4.0, molar ratio) catalysts were synthesized by a facile co-nanocasting method with active carbon as hard template. Typically, a mixture of $Ni(NO_3)_2{\cdot}6H_2O$, $Ce(NO_3)_3{\cdot}6H_2O$ and $ZrOCl_2{\cdot}8H_2O$ was dissolved into deionized water. A certain amount of activated carbon powder was dispersed in the solution and heated to 70 °C. A squirming pump was used to slowly add the Na_2CO_3 solution into the mixture until pH 9-10 under continuous stirring. After being maintained at 70 °C for 2 h, the mixture was strictly filtrated and washed with hot deionized water. The obtained solid was dried in a drying oven at 100 °C overnight and further calcined at 600 °C for 5 h in static air. The obtained catalyst was labelled as NiCeZr-N. Another catalyst was prepared by conventional co-precipitation method. This catalyst was labelled as NiCeZr-P.

3. Catalyst Characterization

The specific surface areas and pore volumes of the samples were measured using a Micromeritics ASAP2010 instrument. Before measurement, catalyst was degassed for 1 h at 300 °C under a N_2 flow to remove the adsorbed impurities.

XRD patterns of the samples were collected on a Shimadzu XRD-7000S with Cu Kα radiation at 40 kV and 100 mA. The diffraction patterns were recorded in the range of $10^{\circ}<2\theta<70^{\circ}$ with a scan speed of 0.3 s·step^{-1} and a step size of 0.03°. The crystal sizes were calculated according to the Scherrer equation [32].

(Scherrer equation: $D=K\gamma/B\cos\theta$, $K=0.89$, $\gamma=0.154056$ nm)

The surface properties of reduced catalyst were characterized by X-ray photoelectron spectroscopy (XPS) on ESCALAB210 instrument. The charge-correction was carried out with a binding energy of C 1s (284.6 eV) as reference, and the spectrum curve was fitted by Gaussian-Lorentzian method.

Elemental analysis was carried out by inductively coupled plasma atomic emission spectroscopy (ICP-AES) operated on a Perkin Elmer Optima 8000 equipment. Sample was dissolved into aqua regia, and then the solution was diluted with HNO_3 to meet the detection limit of the setup. The ICP-AES analysis confirmed the desired composition of the catalyst.

Hydrogen temperature-programmed reduction (H_2-TPR) experiments were carried out in a U-shaped quartz reactor. Prior to the TPR measurements, samples were pretreated at 200 °C for 1 h in flowing Ar (40 mL/min) to remove any moisture and adsorbed impurities. After the reactor was cooled to room temperature, a flow of 5.0% H_2/Ar (40 mL/min) was introduced to reduce the samples. The reaction temperature was increased linearly to 800 °C at a rate of 5 °C/min. The hydrogen consumption was monitored using a thermal conductivity detector (TCD).

Raman spectroscopy measurements were carried out on a Thermo

Table 1. Physicochemical properties of the NiCeZr-P and NiCeZr-N

Catalyst	X_{Ni} [a] (wt%)	Ce/Zr [a] (molar ratio)	S_{BET} [b] (m^2/g)	V_{pore} [b] (cm^3/g)	D_{pore} [b] (nm)	Fresh D_{Ni} [c] (nm)	Used D_{Ni} [c] (nm)
NiCeZr-P	4.63	4.1	24	0.106	15.3	12.5	25.9
NiCeZr-N	4.88	3.97	39	0.157	14.9	---	<5 nm

[a] Calculated from ICP-AES analysis.
[b] Measured by N_2 adsorption-desorption.
[c] Calculated from the XRD patterns (Debye-Scherrer equation).

Scientific DXR Raman microscope using a green laser (λ=532 nm, maximum power 10 mW) with a spot diameter of 0.7 μm and a pinhole aperture of 50 μm. The wavenumber values were measured over the range 100-3,200 cm^{-1} with an average of two scans. The intensity and position were achieved by Lorentzian fitting model [33].

Transmission electronic microscopy (TEM) analysis was performed on a JEM-2100 microscope operating at 200 kV to determin the morphology structure of the samples. Prior to tests, the sample powder was dispersed in ethanol solution by an ultrasonic technique. Then, the resulting suspension was deposited on a copper grid coated with a porous carbon film and the grid was placed in ambient air for ethanol evaporation.

4. Catalytic Tests

DRE reaction was conducted in a continuous-flow fixed-bed reactor. 100 mg catalyst (40-60 mesh) were mounted in the reactor and sandwiched between two layers of quartz wool. The catalyst was then reduced under 5% H_2/N_2 mixture (40 mL·min^{-1}) at 500 °C for 1 h. The experimental parameters were as follows: $C_2H_5OH/CO_2/N_2$=1/1/2 (molar ratio), the gas hourly space velocity (GHSV)=27,000 mL·g^{-1} h^{-1}. The products were monitored by online gas chromatography. H_2, N_2, CO, CH_4 and CO_2 were separated using a packed column and analyzed using a thermal conductivity detector (TCD). Acetaldehyde, acetone and ethanol were separated using a capillary column and analyzed using a flame ionization detector (FID).

Ethanol conversion (EC) was calculated based on:

$$EC\ (\%)=[(C_{EtOH})_{in}-(C_{EtOH})_{out}]/(C_{EtOH})_{in}\times 100 \qquad (1)$$

with $(C_{EtOH})_{in}$ and $(C_{EtOH})_{out}$ referring to the inlet and outlet molar flows of ethanol.

Molar concentrations of the products in the outlet gas were calculated based on:

$$S_x(\%)=(M_x)_{outlet}/\Sigma(M_i)_{outlet} \qquad (2)$$

where $(M_x)_{outlet}$ is the moles of products (labeled as x) in the outlet gas including H_2, CO, CO_2, CH_4, acetaldehyde, acetone.

RESULTS AND DISCUSSION

1. Characterization

The physicochemical properties of the as-prepared catalysts are listed in Table 1. The ICP results show that the actual content of active metal was close to the nominal one, and the molar ratio of Ce/Zr was also consistent with the targeted value. The result of multi-BET indicated that the specific surface area of NiCeZr-P was 24 m^2/g. On the contrary, NiCeZr-N prepared by co-nanocasting method was as high as 39 m^2/g, and NiCeZr-N exhibited larger pore volume and smaller pore diameter. The results obtained by XRD depicted that NiCeZr-N had a smaller grain size, which normally led to better catalytic activity. This finding was in line with the reported literature that co-nanocasting technique could inhibit the aggregation of the particle during synthesis process. Indeed, nanocasting technology might make use of the spatial limited properties of hard templates to restrict the aggregation of the particles and achieve catalysts with small grain size and relatively high surface area, thus improving catalyst activity.

The particle size and dispersion of catalysts could be also inferred by TEM. As shown in Fig. 1, the relative particle size of NiCeZr-N was smaller than that of NiCeZr-P, thereby indirectly suggesting its higher dispersion. The results were consistent with the results of XRD analysis.

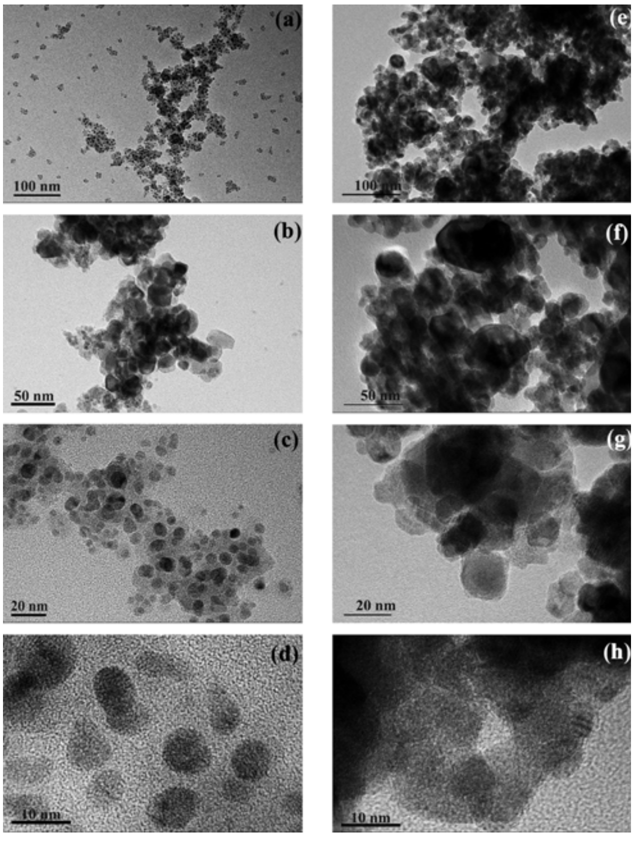

Fig. 1. TEM images of the fresh catalysts: (a)-(d) NiCeZr-N and (e)-(h) NiCeZr-P.

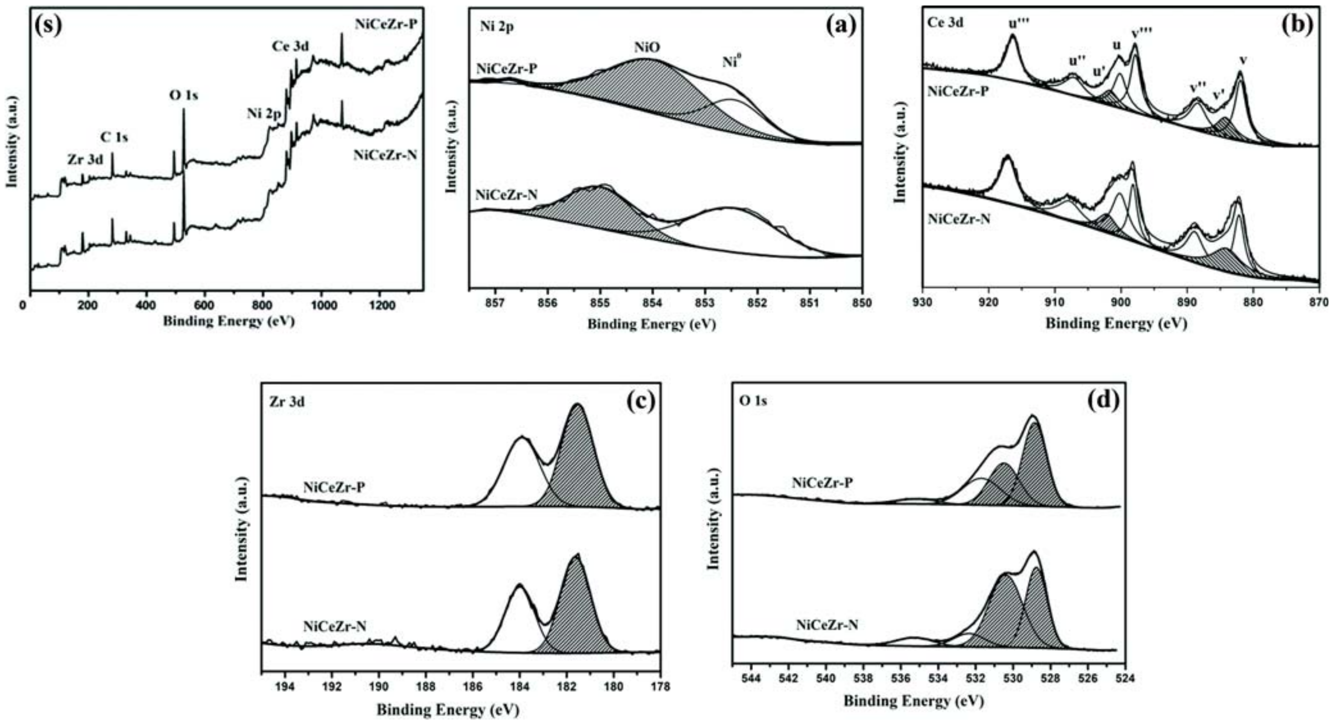

Fig. 2. XPS spectra of reduced catalysts: (s) NiCeZr-N and NiCeZr-P; (a) Ni 2p; (b) Ce 3d; (c) Zr 3d and (d) O 1s.

The survey spectra of the two samples are shown in Fig. 2. XPS survey scan clearly confirmed the presence of elements Ni, Ce, Zr and O in all cases. Fig. 2(a)-(d) demonstrates the chemical state of surface Ni, Ce, Zr and O species in the reduced catalysts. As displayed in Fig. 2(a), the Ni^0 species was noted on the reduced samples. However, for NiCeZr-N catalysts, the Ni^0 species accounts for a larger proportion of the catalysts. The observation of the NiO species might be attributed to the reoxidation of the metallic Ni^0 species due to the ex-situ reduction process. According to the peak area formula, the proportion of Ni^0 NiCeZr-N catalyst was ca. 58%, while the proportion of Ni^0 in the NiCeZr-P catalyst was only about 27%. This result might be explained by the fact that the strong Ni-support interaction in NiCeZr-N sample could efficiently inhibit the reoxidation of Ni^0 sites.

The Ce 3d spectrum was composed of two multiplets (v and u) corresponding to 3d5/2 and 3d3/2 core holes, respectively, for spin-orbit splitting in Fig. 2(b) [34]. The binding energy peaks (denoted as u‴ (917.1 eV), u″ (907.3 eV), u (901.5 eV), v (883.0 eV), v″ (888.7 eV) and v‴ (898.5 eV)) evidenced the presence of Ce^{4+} species. On the other hand, the bands (denoted as u′ (903.6 eV) and v′ (885.4 eV)) corresponded to the Ce^{3+} sites, which was consistent with the results reported in the literature [34,35]. It was well known that the more Ce^{3+} in the composition, the more defects formed in CeO_2 framestructure, which would be conducive to the formation of oxygen vacancies in the catalyst.

Therefore, by calculating the relative ratio of Ce^{4+} and Ce^{3+}, the relative concentration of oxygen vacancy in the catalyst was obtained [36]. Results indicated that NiCeZr-N catalyst (22.5% contained more oxygen vacancies) than the value of NiCeZr-P catalyst (16.1%), which can effectively improve the catalyst activity.

Fig. 2(c) shows the XPS spectra of Zr 3d on NiCeZr-P and NiCeZr-N catalysts, respectively. The characteristic peak at 182.5 eV was attributed to Zr 3d [35].

Fig. 2(d) shows the O1s XPS spectra of NiCeZr-P and NiCeZr-N catalysts, respectively. Particularly, the O1s curve fitting indicated that the two peaks (528.5 eV and 529.8 eV) were, respectively, attributed to lattice oxygen and chemisorbed oxygen [37]. This mobile lattice oxygen species could promote the activation of C-H bonds.

The XRD pattern of the fresh catalysts is presented in Fig. 3. XRD standard spectra of NiO and CeO_2 phases are aslo listed in Fig. 3, which is convenient for the analysis of XRD spectra. The

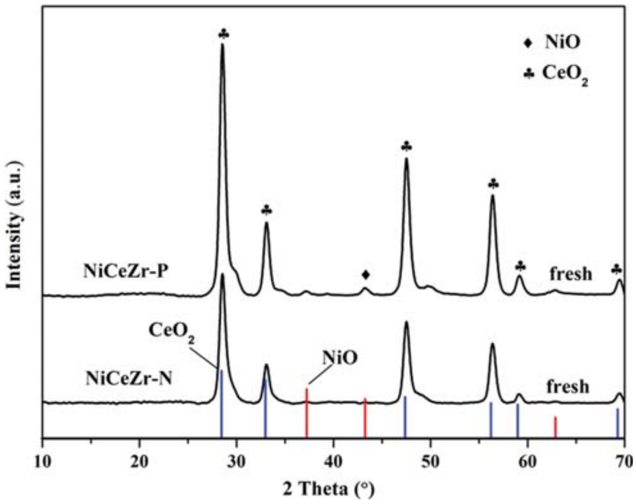

Fig. 3. XRD patterns of the fresh NiCeZr-P and NiCeZr-N.

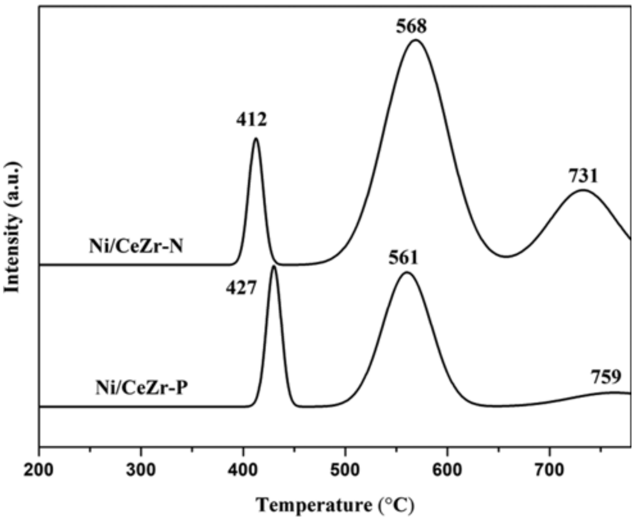

Fig. 4. H_2-TPR profiles of fresh NiCeZr-P and NiCeZr-N.

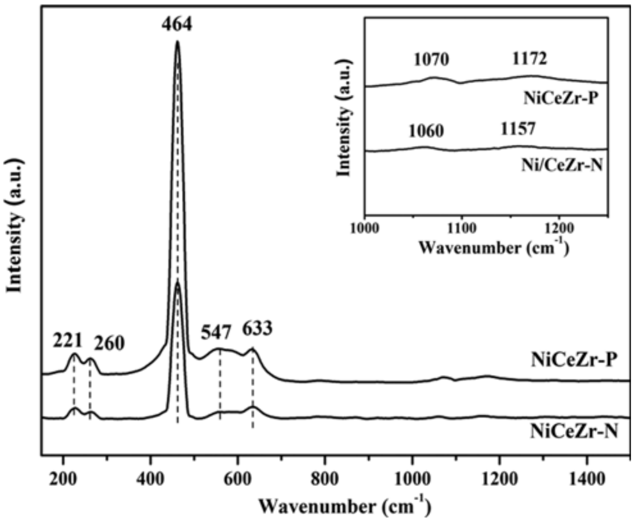

Fig. 5. Raman spectra of the fresh NiCeZr-P and NiCeZr-N.

peaks at 28.6°, 33.1°, 47.5°, 56.4°, 59.1° and 69.5° were assigned to the diffraction bands of CeO_2 (JCPDS 34-0394). Noticeably, it was observed that peak position was slightly shifted to a large angle in comparison to the pure CeO_2, indicating that the addition of Zr caused a slight effect on the lattice size of CeO_2. Weak peaks at 37.2°, 43.3° and 62.9° corresponding to NiO species (JCPDS 47-1049) were noted in NiCeZr-P sample. However, these small peaks were not observed in NiCeZr-N. The result indicated that the co-nanocasting method ensured the active metal with the relatively higher dispersion.

H_2-TPR profiles of NiCeZr-P and NiCeZr-N are shown in Fig. 4. For NiCeZr-N, the peak at 412 °C was attributed to the reduction peak of the NiO particles [38]. The peak at position 568 °C was considered to be the reduction peak of surface CeO_2; and the peak above 700 °C might correspond to the reduction peak of the bulk CeO_2, which was difficult to be reduced to Ce^{3+} species at low temperature [39]. Interestingly, the intensity of the reduction peak for NiCeZr-N catalyst at about 560 °C was stronger than that of NiCeZr-P, indicating that more CeO_2 was reduced in NiCeZr-N, thereby with the higher oxygen storage capacity. Because ZrO_2 was difficult to be reduced under 900 °C conditions, there was no reduction peak of ZrO_2 in the figure [40]. Compared with NiCeZr-P, the reduction peak of NiCeZr-N shifted to the lower temperature at about 400 °C, indicating that NiO particle size in NiCeZr-N was smaller and easier to be reduced.

The calculated H_2 consumption based on standard CuO method was as follows: NiCeZr-P (0.98 mmol/g)<NiCeZr-N (1.70 mmol/g). Combined with the ICP analysis results, the actual hydrogen consumption of the two catalysts exceeded the theoretical hydrogen consumption required to reduce NiO oxide to Ni^0. The excess hydrogen might be attributed to the reduction of CeO_2. The reduction degree of CeO_2 was then calculated to depict the formed Ce^{3+} species in CeO_2 oxide. For NiCeZr-N catalyst, the extra hydrogen further reduced CeO_2 to $CeO_{1.88}$. In the NiCeZr-P catalyst, CeO_2 was reduced to $CeO_{1.97}$. The results indicated that more Ce^{4+} sites in NiCeZr-N were reduced into Ce^{3+} species compared to the value of NiCeZr-P sample. Generally, the number of Ce^{3+} sites was somehow correlated with the O vacancies. Indeed, additional O defects were necessary to guarantee electrical neutrality, suggesting that Ce^{3+} ions facilitated the existence of oxygen vacancies. H_2-TPR results indirectly evidenced the existence of more oxygen defects in NiCeZr-N catalyst. Apart from this, oxygen defects were favorable for the adsorption/activation of CO_2 to form the active O species, which was favorable to improve the catalyst activity and stability in dry reforming process. In addition, it accelerated the diffusion of bulk oxygen to CeO_2 surface and the surface transfer of O species, which was favorable for the in-situ elimination of the carbon over the catalyst surface. Therefore, Ce^{3+}-riched sample might possess better catalytic performance for ethanol dry reforming.

Fig. 5 shows the Raman spectra of the synthesized catalysts. In all cases, a characteristic peak at 464 cm^{-1} was assigned to CeO_2 with fluorite structure [41]. Moreover, compared with pure CeO_2, the position of the absorption peak shifted to the higher region, which was probably due to the change of lattice structure during the formation of CeZr solid solution. Particularly, another band at ca. 633 cm^{-1} corresponded to the asymmetric vibration of oxygen vacancies in the catalyst, which evidenced the formation of defects in the crystal structures of NiCeZ-P and NiCeZr-N [42]. No obvious peak related to NiO was noted in the Raman spectra of all samples. This could be explained by the fact that the Raman diffuse reflection of NiO was too weak to be detected at this scale [43]. According to the literature [42], the relative concentration of oxygen vacancies on catalyst was usually calculated by the peak area ratio at 547 cm^{-1} and 460 cm^{-1} (A_{547}/A_{460}). The obtained value for NiCeZr-N (0.067) was higher than the value of NiCeZr-P (0.051). Hence, the results revealed that NiCeZr-N can provide more oxygen defect sites, thereby enhancing the catalyst activity. Compared with CeZr support, a slight change of the weak band at 260 cm^{-1} occurred. It might be related to crystal defects due to the incorporation of Ni species into CeO_2 lattice [39].

Generally, the peaks at ca. 1,172 and 1,157 cm^{-1} were ascribed to the primary asymmetry of CeO_2. The weak band at 221 cm^{-1} corresponded to the asymmetric vibrations due to the formation of oxygen vacancies [44].

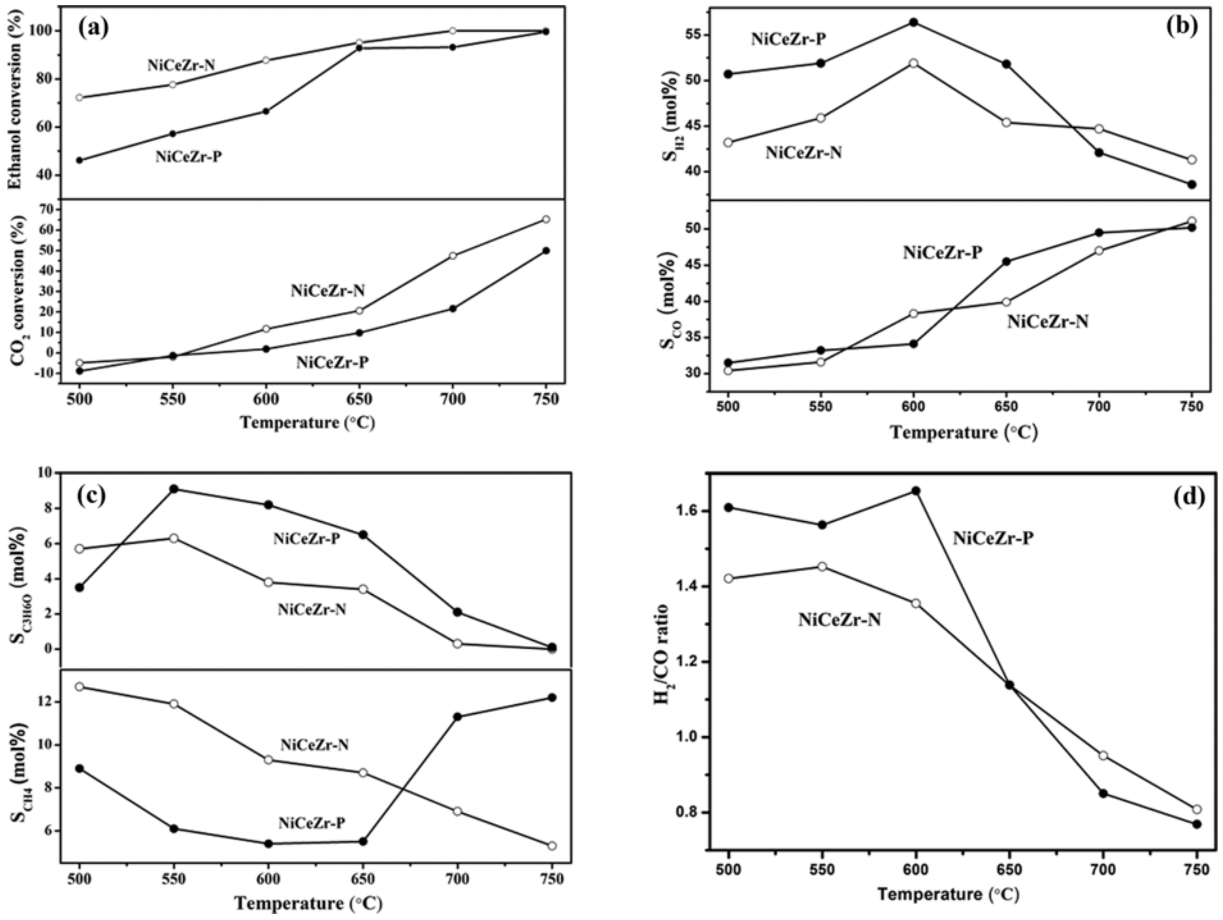

Fig. 6. Effect of reaction temperature on the product distribution for DRE over NiCeZr-P and NiCeZr-N. Reaction conditions: Ethanol/CO_2=1/1; GHSV=27,000 mL·g^{-1}·h^{-1}.

2. Catalytic Tests

The performance of two catalysts in DRE reaction at different temperatures is illustrated in Fig. 6. As depicted in Fig. 6(a), ethanol conversion in all cases increased upon increasing reaction temperature, while the ethanol conversion rate on NiCeZr-N was always higher than that on NiCeZr-P before 650 °C. Upon heating to 700 °C, ethanol was completely converted, while it was only 750 °C for NiCeZr-P catalyst.

At below 550 °C, the calculated CO_2 conversion was always a negative value, indicating that the decomposition of ethanol into CO_2 might occur. With further increasing temperature to 750 °C, CO_2 conversion of NiCeZr-N and NiCeZr-P increased to 65.3% and 49.9%, respectively.

With respect to H_2 selectivity (Fig. 6(b)), both catalysts first increased with the maximum value at 600 °C and then decreased at the higher temperature. The observed decline explained the occurrence of the reverse water gas shift reaction (CO_2+H_2→CO+H_2O) [1,17]. This was further evidenced by the increase of the CO selectivity at higher temperature.

Fig. 6(c) shows the concentrations of the by-products (C_3H_6O and CH_4). In the case of C_3H_6O, its formation was obviously prevented at higher temperature. For NiCeZr-N sample, methane selectivity also declined with increasing temperature. This may have been due to the occurrence of methane dry reforming (CH_4+CO_2→2CO+2H_2), which is favorable at higher temperature.

However, the drastic increase of methane at above 650 °C indirectly depicted that NiCeZr-P catalyst exhibited limited activity for methane dry reforming.

The ratio of H_2/CO at different temperature is also shown in Fig. 6(d). It can be seen that the value of H_2/CO was close to 1.1 at 650 °C, which basically meets the requirements of the ratio of H_2 to CO for Fischer-Tropsch synthesis. On the whole, the fluctuation range of H_2/CO value of NiCeZr-N was smaller, thereby suggesting that NiCeZr-N was more suitable than NiCeZr-P to synthesize the feedstocks for Fischer-Tropsch process.

For a clear comparison, some reported catalysts for DRE are summarized in Table S1. Among them, NiCeZr-N catalyst (5%Ni/$CeZrO_2$, co-nanocasting) had higher ethanol conversion compared with the other transition metal based catalysts such as 3%Ce-10% Ni/Al_2O_3, 10% Ni/Al_2O_3, 3%La-10%Co/Al_2O_3. Moreover, NiCeZr-N catalyst exhibited comparable activity with the noble-based catalysts (1% Rh/CeO_2 and 2% Ir/CeO_2). Hence, NiCeZr-N catalyst might be one of the promising alternatives for ethanol dry reforming.

The stability results of the as-prepared catalysts at 600 °C for 40 h in Fig. 7 indicate that ethanol conversion of NiCeZr-N sample was still maintained during 40 h of reaction, indicating that co-nanocasting method with activated carbon as hard template could improve the ability of the catalyst to resist carbon deposition and effec-

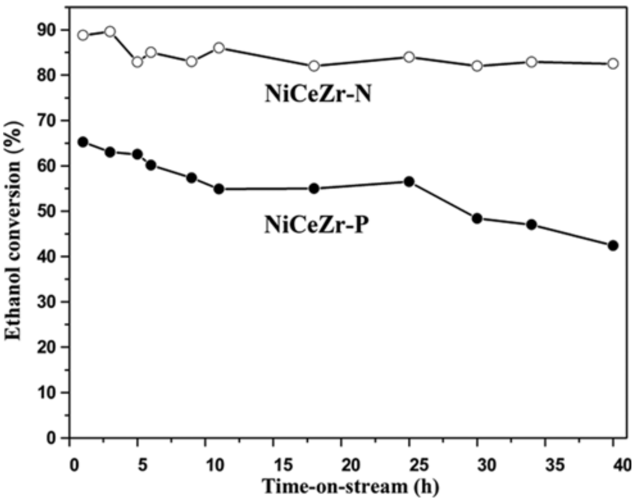

Fig. 7. Stability test for DRE reaction at 600 °C; Reaction conditions: Ethanol/CO_2=1/1; GHSV=27,000 mL·g^{-1}·h^{-1}.

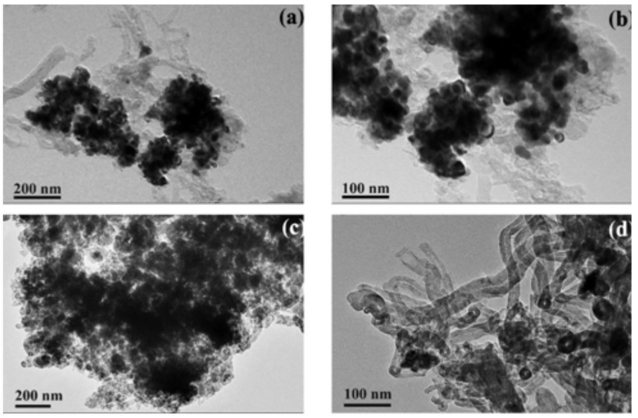

Fig. 8. TEM images of the the spent cayalysts: (a), (b) NiCeZr-N and (c), (d) NiCeZr-P.

tively alleviate the sintering of the active component even under serious reaction conditions. However, ethanol conversion for NiCeZr-P catalyst decreased rapidly after a period of reaction, and the conversion value declined to ca. 40% after 40 h of reaction, indicating its unsatisfactory stability.

3. Characterization of Spent Catalyst

Fig. 8 shows TEM image of the spent catalysts (NiCeZr-P and NiCeZr-N). After the reaction at 600 °C for 40 h, the particle sizes of NiCeZr-P catalyst increased obviously, and meanwhile serious carbon deposition occured. In terms of morphology, carbon deposition mainly consisted of fibrous carbon and a type of encapsulated coke [43]. Note that the encapsulated carbon in NiCeZr-P sample, which was more harmful for catalyst activity, covered most of the catalyst surface. On the other hand, NiCeZr-N catalyst had strong oxygen atom supply capacity, which can effectively eliminate carbon accumulation during the reaction process. Therefore, NiCeZr-N catalyst can maintain stable activity.

As presented in Fig. 9, carbon peaks attributed to Graphite-2H (JCPDS 41-1487) appeared at around 26.4° [42,43]. It can be seen that the smaller peaks for NiO are observed for NiCeZr-N (<5 nm).

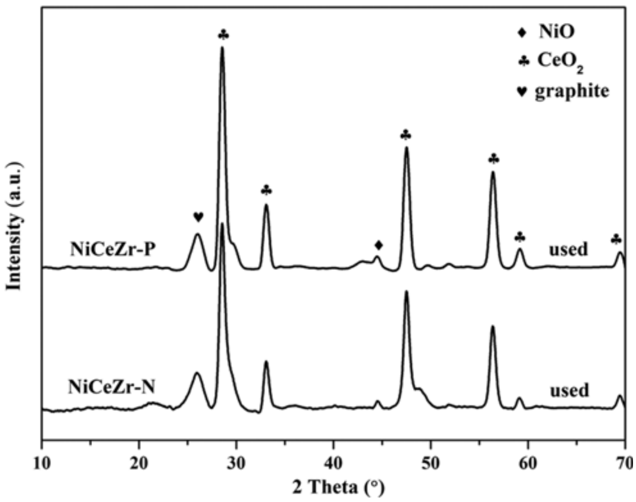

Fig. 9. XRD patterns of the spent NiCeZr-P and NiCeZr-N.

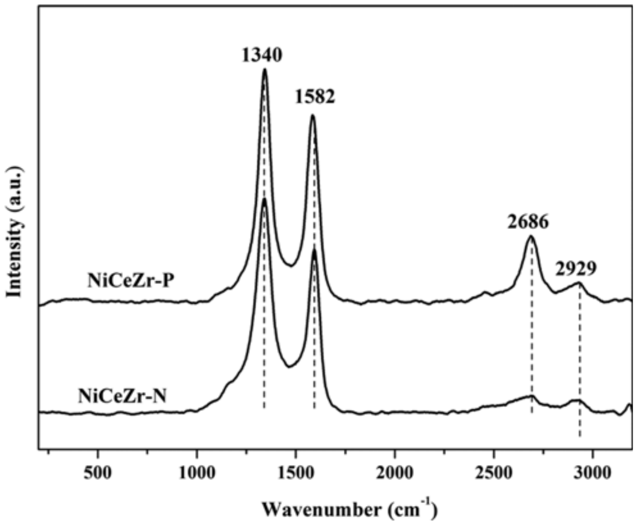

Fig. 10. Raman spectra of the used NiCeZr-P and NiCeZr-N.

On the contrary, the crystal particle size of the aged NiCeZr-P catalyst remarkably increased to 25.9 nm. The results showed that the catalysts agglomerated to some extent after the stability tests, and the particle size of the active metal increased.

Raman spectra of the used catalysts are shown in Fig. 10. The three peaks at ca. 1,340, 1,582 and 2,686 cm^{-1}, respectively, represented the characteristic peaks of carbon materials with different structure [44,45]. The G band at 1,582 cm^{-1} can indicate the presence of carbon deposition with an ordered structure (sp2 network). Generally, this type of coke led to catalyst deactivation. However, D band at about 1,340 cm^{-1} revealed the formation of the amorphous carbon with low crystalline, which had the less impact on catalyst activity. Note that the peak at 2,686 cm^{-1} was assigned to an octave peak of 1,340 cm^{-1}, thereby the spectral band here was commonly called 2D band [45]. Moreover, Raman band at about 2,929 cm^{-1} was probably attributed to the combination of D band and G band [44].

In previous studies, the ratio of peak area of the D band and the

G band (I_D/I_G) was calculated to define the degree of carbon crystallization in the catalyst, thus further representing the degree of carbon deposition. The calculated I_G/I_D values obeyed the following rank: NiCeZr-P (0.70)>NiCeZr-N (0.54). Therefore, it can be seen that the surface of NiCeZr-P was covered by more carbon deposition, resulting in its rapid deactivation.

CONCLUSION

The experimental results revealed that NiCeZr-N catalyst prepared by co-nanocasting method exhibited better activity and stability in comparison with NiCeZr-P synthesized by the conventional co-precipitation method. Typically, co-nanocasting method can effectively reduce the size of the active metal, thereby increasing its dispersion. On the other hand, these positive factors could effectively alleviate coke deposition and the sintering of active metal during a reaction. Herein, the catalyst prepared by co-nanocasting method showed a potential application in syngas production from ethanol dry reforming.

ACKNOWLEDGEMENTS

This work was supported by Liaoning Provincial Natural Science Foundation of China (grant No. 2019-ZD-0293).

SUPPORTING INFORMATION

Additional information as noted in the text. This information is available via the Internet at http://www.springer.com/chemistry/journal/11814.

REFERENCES

1. S. Bac, S. Keskin and A. K. Avci, *Sust. Energy Fuels*, **4**, 1029 (2020).
2. F. Fayaz, L. G. Bach, M. B. Bahari, T. D. Nguyen, K. B. Vu, R. Kanthasamy, C. Samart, C. Nguyen-Huy and D. N. Vo, *Int. J. Energy Res.*, **43**, 405 (2018).
3. S. Kumar and M. K. Mondal, *Korean J. Chem. Eng.*, **37**, 231 (2020).
4. J. Yu, J. A. Odriozola and T. R. Reina, *Catalysts*, **9**, 1015 (2019).
5. O. A. López, S. R. Pallares, Z. M. J. Meléndez and V. Collins-Martínez, *Int. J. Hydrogen Energy*, **40**, 17172 (2015).
6. A. Zwadzki, J. D. A. Bellido, A. F. Lucrédio and E. M. Assaf, *Fuel Process. Technol.*, **128**, 432 (2014).
7. C. Dang, S. Wu, G. Yang, Y. Cao, H. Wang, F. Peng and H. Yu, *J. Energy Chem.*, **43**, 90 (2020).
8. S. Zhao, W. Cai, Y. Li, H. Yu, S. Zhang and L. Cui, *J. Saudi Chem. Soc.*, **22**, 58 (2018).
9. A. Drif, N. Bion, R. Brahmi, S. Ojala, L. Pirault-Roy, E. Turpeinen, P. K. Seelam, R. L. Keiski and F. Epron, *Appl. Catal. A*, **504**, 576 (2015).
10. E. L. Saché, L. Pastor-Pérez, D. Watson, A Sepúlveda-Escribano and T. R. Reina, *Appl. Catal. B: Environ.*, **236**, 458 (2018).
11. S. Jo and Y. Kim, *Korean J. Chem. Eng.*, **11**, 3203 (2016).
12. M. B. Bahari, F. Fayaz, N. Ainirazali, N. H. H. Phuc and D.-V. N. Vo, *Arpn J. Eng. Appl. Sci.*, **11**, 7249 (2016).
13. K. Samsudeen, A. F. Ahmed, M. Yahya, A. Ahmed and F. Anis, *Int. J. Res. Sci.*, **4**, 5 (2018).
14. Q. Zhang, J. Wang, P. Ning, T. Zhang, M. Wang, K. Long and J. Huang, *Korean J. Chem. Eng.*, **34**, 2823 (2017).
15. O. Daoura, M.-N. Kaydouh, N. Ei-Hassan, P. Massiani, F. Launay and M. Boutros, *J. CO_2 Util.*, **24**, 112 (2018).
16. H. Li, Y. Qiu, C. Wang, X. Huang, T. Xiao and Y. Zhao, *Catal. Today*, **317**, 76 (2018).
17. B. Bej, S. Bepari, N. C. Pradhan and S. Neogi, *Catal. Today*, **291**, 58 (2017).
18. Z. Li, Z. Wamg, B. Jiang and S. Kawi, *Catal. Sci. Technol.*, **8**, 3363 (2018).
19. Y. Wei, W. Cai, S. Deng, Z. Li, H. Yu, S. Zhang, Z. Yu, L. Cui and F. Qu, *Renew. Energy*, **145**, 1507 (2020).
20. E. Delahaye, V. Escax, N. E. Hassan, A. Davidson, R. Aquino, V. Dupuis, R. Perzynski and Y. L. Raikher, *J. Phys. Chem. B*, **110**, 26001 (2006).
21. W. Tang, X Wu, S. Li, X. Shan, G. Liu and Y. Chen, *Appl. Catal. B: Environ.*, **162**, 110 (2015).
22. M. M. Nair, S. Kaliagunine and F. Kleitz, *ACS Catal.*, **4**, 3837 (2014).
23. B. Huang, C. H. Bartholomew and B. F. Woodfield, *Micropor. Mesopor. Mater.*, **183**, 37 (2014).
24. Q. Duan, J. Wang, C. Ding, H. Ding, S. Guo, Y. Jia, P. Liu and K. Zhang, *Fuel*, **18**, 112 (2017).
25. T. Valdés-Solís, G. Marbán and A. B. Fuertes, *Catal. Today*, **116**, 354 (2006).
26. F. F. Sousa, H. S. A. Sousa, A. C. Oliveira, M. C. C. Junior, A. P. Ayala, E. B. Barros, B. C. Viana, J. M. Filho and A. C. Oliveira, *Int. J. Hydrogen Energy*, **37**, 3201 (2012).
27. T. Xu, J. Zou, W. Tao, S. Zhang, L. Cui, F. Zeng, D. Wang and W. Cai, *Fuel*, **183**, 238 (2016).
28. A. S. Deshpande and M. Niederberger, *Micropor. Mesopor. Mater.*, **101**, 413 (2007).
29. P. S. Bulutoglu, Z. Say, S. Bac, E. Ozensoy and A. K. Avci, *Appl. Catal. A: Gen.*, **564**, 157 (2018).
30. J. Guerrero-Caballero, T. Kane, N. Haidar, L. Jalowiecki-Duhamel and A. Löfberg, *Catal. Today*, **333**, 251 (2019).
31. F. Basile, R. Mafessanti, A. Fasolini, G. Fornasari, E. Lombardi and A. Vaccari, *J. Eur. Ceram. Soc.*, **39**, 41 (2019).
32. B. D. Culity, *Elements of X-ray diffraction*, Addison-Wesley Metallurgy Series, Boston (1978).
33. J. R. Mcbride, K. C. Hass, B. D. Poindexter and W. H. Weber, *J. Appl. Phys.*, **76**, 2435 (1994).
34. Y. Wang, L. Yao, Y. Wang, S. Wang, Q. Zhao, D. Mao and C. Hu, *ACS Catal.*, **8**, 6495 (2018).
35. H. Xu, M. Sun, S. Liu, Y. Li, J. Wang and Y. Chen, *Rsc. Adv.*, **7**, 24117 (2017).
36. E. Bêche, P. Charvin, D. Perarnau, S. Abanades and G. Flamant, *Surf. Interface Anal.*, **40**, 264 (2008).
37. A. Horvath, W. Cai, N. Homs and P. R. Piscina, *Appl. Catal. B: Environ.*, **150-151**, 47 (2014).
38. M. Cai, J. Wen, W. Chu, X. Cheng and Z. Li, *J. Natural Gas Chem.*, **20**, 318 (2011).
39. A. Horváth, G. Stefler, O. Geszti, A. Kienneman, A. Pietraszek and L. Guczi, *Catal. Today*, **169**, 102 (2011).
40. P. C. Zonetti, S. Letichevsky, A. B. Gaspar, E. F. Sousa-Aguiar and L. G. Appel, *Appl. Catal. A: Gen.*, **475**, 48 (2014).

41. X. Gao, G. Liu, Q. Wei, G. Yang, M. Masaki, X. Peng, R. Yang and N. Tsubaki, *Int. J. Hydrogen Energy*, **42**, 26 (2017).
42. Y. L. Wu, W. J. Zhao, X. H. Li and W. Y. Li, *J. Fuel Chem. Technol.*, **5**, 189 (2017).
43. V. Pawar, D. Ray, C. Subrahmanyam and V. M. Janardhanan, *Energy Fuels*, **29**, 8047 (2015).
44. M. A. Pimenta, G. Dresselhaus, M. S. Dresslhaus, L. G. Cancado, A. Jorio and R. Saito, *Phys. Chem. Chem. Phys.*, **9**, 1276 (2007).
45. Y. Hao, Y. Wang, L. Wang, Z. Ni, Z. Wang, R. Wang, C. K. Koo, Z. Shen and J. T. L. Thong, *Small*, **6**, 195 (2010).